Flow and Heat Transfer from a Rotating Sphere Partially Immersed in a Bounded Stationary Fluid

Safarzadeh, Sajjad; Baradaran Rahimi, Asghar*[+]

Faculty of Engineering, Ferdowsi University of Mashhad, Mashhad, I.R. IRAN

ABSTRACT: *For the first time, a numerical study has been carried out to investigate the flow and heat transfer from a partially immersed rotating sphere in a bounded boundary stationary fluid with variable distances from its surface. The simulations are performed for different boundary distances under various types of rotational speed of the sphere using the two-phase VOF model. The flow and thermal fields are investigated through streamlines, isotherm, and volume fraction contours, as well as through the average Nusselt number and the thickness of the water film. The numerical results demonstrate that the water is drawn up the sphere's lower pole because of the centrifugal force generated by the rotation, and its motion continues due to the water film formation. Then, the water film is radially thrown out because of the inertial forces dominance. Moreover, the sinusoidal pulsation rotational speed indicates higher heat transfer performance among various functions. Compared with the exponential function by increasing the boundary radius from $R_\infty = 7$ cm to $R_\infty = 10$ cm the time-surface-averaged Nusselt number increases by about 35%. Also, it is found that as the immersion angle increases from $\theta_i = 30°$ to $\theta_i = 60°$, surface-averagedusselt number increases by about 51% on average for the uniform rotational speed of the sphere.*

KEYWORDS: *Rotating sphere, VOF model, Bounded boundary, Heat transfer, Immersion angle.*

INTRODUCTION

A numerical investigation of convective heat transfer from a partially immersed rotating sphere with constant and time-dependent angular velocities around the vertical axis is considered. Variable radius in a rotating sphere causes fluid to be pulled upwards and ejected radially. However, the occurrence of this event in the case of partial immersion requires special conditions. In the case of a partially immersed rotating sphere, the formation of a primary meniscus on the sphere's surface is necessary. The necessary condition for the formation of this primary meniscus is that the contact angle between the liquid film and the surface of the sphere is less than 90 degrees, in which case the surface of the sphere is called hydrophilic [1]. This performance is similar to the Von Karmán viscous pump, which rotates in an infinite fluid [2]. Also, this mechanism is used in many technological applications such as mixers, fluid gyroscopes, centrifuges, and geophysics. One of the most important engineering applications of this mechanism is a scavenging pump that is used for the evacuation of liquid from the tank floor.

Many researchers have studied the convective heat transfer from fixed or rotating objects [3-14]. Several studies have investigated the flow and heat transfer from a rotating cylinder [15-21]. *Alsabery et al*. [15] numerically investigated the mixed convection heat transfer from a heated rotating cylinder inside a cavity. Their results

* *To whom correspondence should be addressed.*
+E-mail address: rahimiab@um.ac.ir
1021-9986/2023/4/1329-1342 14/$/6.04

showed that the maximum values of the mean Nusselt number are achieved when the heated circular cylinder rotates counter-clockwise. *Wang et al*. [16] numerically studied the periodic transient mixed convection heat transfer from a hot rotating cylinder within an enclosure. According to their results, the heat transfer rate in time-periodic transient mixed convection is higher than steady-state ones. In another numerical investigation, *Liao* and *Lin* [17] evaluated the effect of a hot rotating cylinder on free and mixed convection inside an enclosure. Based on their results, the stability of the flow within the enclosure is affected by cylinder rotation. *Sasmal et al*. [18] numerically examined the effect of a hot rotating cylinder on laminar free convection in a duct containing a power-law fluid. Their results indicated that the heat transfer rate increases with increase in the angular velocity of the cylinder at low Rayleigh numbers. Mixed convection heat transfer and turbulent flow around an insulated rotary cylinder inside a lid-driven cavity are numerically investigated by *Kareem* and *Gao* [19]. They reported that the temperature fields and streamline patterns are highly dependent on the cylinder angular velocity. In a 3D numerical investigation, *Selimefendigil* and *Öztop* [20] studied the mixed convection heat transfer from two adiabatic rotating cylinders inside a cavity containing different nanofluids. They developed a relation for the mean Nusselt number in terms of cylinder rotational speed and Rayleigh number.

Several investigations have studied the convective heat transfer around a rotating sphere [22-30]. *Souayeh et al*. [22] numerically investigated the free convection from a heated sphere inside an enclosure. They suggested a correlation for the mean Nusselt number of the heated inner sphere. Moreover, they compared the cylindrical and spherical shapes of the inner object and reported that the heat transfer rate increases using the spherical shape. In another 3D numerical study, *Lee et al*. [23] evaluated the effect of Rayleigh number and chamber shape on the free convection from a hot spherical surface inside a rectangular enclosure. They proposed a relation for estimation of the Nusselt number in terms of chamber shape and Rayleigh number. *Gallegos* and *Málaga* [24] numerically investigated the free convection heat transfer inside an eccentric spherical annulus. According to their results, when the temperature difference between inner and outer spherical boundaries increases, a transition occurs for the energy transport regime from a conductive regime to a steady convective one. *Chen et al*. [25] numerically studied the combination of natural and forced convection between a rotating sphere and a rectangular chamber. Their results indicated that the heat transfer rate increases due to the rotation of the sphere. The transient free convection flow around a rotating sphere was analytically investigated by *D'Alessio* [26]. In his work, the heat transfer coefficient was calculated at high Grashof numbers.

Many researchers have investigated the case of a fully immersed rotating sphere [31-35]. *Nigam* [31] analytically studied the laminar boundary layer flow from a fully immersed rotating sphere. In his investigation, the velocity distribution and the boundary layer thickness were obtained using a power series solution method. In another analytical study, *Singh* [32] calculated the temperature distribution and the thermal boundary layer thickness of previous work using the power series solution method. *Samad* and *Garrett* [33] analytically and numerically investigated the laminar boundary layer flow on a fully immersed rotating spheroid. Their theoretical solution results were in good agreement with the numerical ones. Convective heat transfer from a fully immersed rotating sphere was analytically and numerically studied by *Kreith et al*. [34]. According to their results for various fluids, the boundary layer thickness increases with increase in the angular distance from the sphere poles. *Feng* [35] numerically investigated the laminar forced convection from a fully immersed rotating sphere. In his study, the flow patterns and the average Nusselt numbers were obtained for the Reynolds numbers between 0 and 1000.

Although several investigations have evaluated the convection heat transfer from a rotating sphere, few of them have examined a partially immersed rotating sphere [1, 36-38]. *Martinez et al*. [37] theoretically investigated a rotating sphere partially immersed inside propylene glycol and water as two fluids with high and low viscosities, respectively. They argued that the main reason for liquid film motion on the sphere's surface is the Coriolis force. In an analytical and experimental study, *Langley et al*. [1] investigated the flow induced by a partially immersed rotating sphere. Based on their results for the Reynolds numbers between 7000 and 370000, the flow rate increases with increase in the rotational speed, fluid viscosity, and immersion angle.

To the authors' best knowledge, the investigation of convection heat transfer around a partially immersed rotating sphere has rarely been the subject of a numerical

Table 1: physical parameters of simulation cases.

Case number	Sphere radius R (cm)	Boundary radius R_∞ (cm)	Immersion angle θ_i (°)	Contact angle θ_c (°)	Surface Temperature T_s (K)
Case 1	5	10	45	40	333.15
Case 2	5	8	45	40	333.15
Case 3	5	7.5	45	40	333.15
Case 4	5	7	45	40	333.15

Table 2: Thermophysical properties of two fluids (at 293.15 [k]).

Thermophysical properties	ρ (kg/m³)	μ × 10³ (kg/m.s)	σ (N/m)	C_p (J/kg.K)	k (W/m.K)	T_∞ (K)
Liquid: Water	998.2	1.003	0.073	4182	0.6	298.15
Gas: Air	1.225	0.017894		1006.43	0.0242	298.15

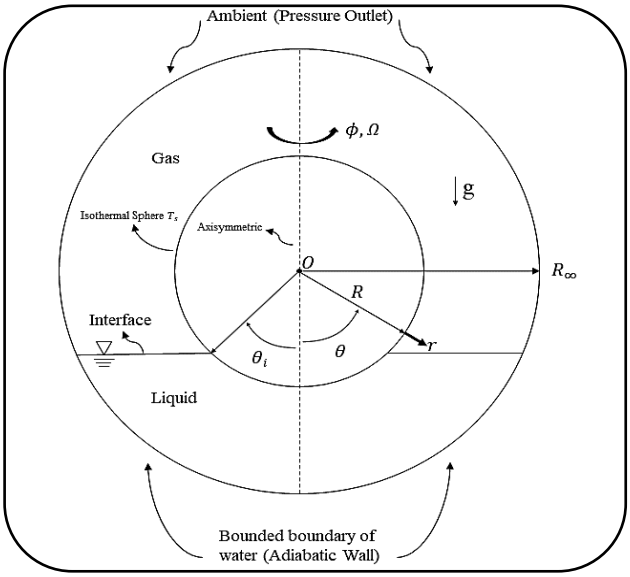

Fig. 1: Schematic of the problem.

simulation. In addition, no research has been found that surveyed the effect of wall distance on the heat transfer rate of the heated surface of a rotating sphere. For the first time, this study is numerically evaluated the flow and heat transfer from a partially immersed rotating sphere in a bounded boundary fluid with variable distances from the sphere's surface. The simulations are performed for different boundary distances under various types of rotational speed of the sphere using the two-phase VOF model. In this paper, the results of various cases are shown by streamlines, isothermal lines, volume fraction contours, and the variations of the Nusselt number and water film thickness.

THEORETICAL SECTION

Geometry description

The problem geometry considered in the spherical coordinate (r, θ, ϕ) is illustrated in Fig. 1, along with the important boundary conditions. The system consists of an inner solid sphere of radius R partially immersed within a bounded boundary of water with a variable radius of R_∞. The inner sphere rotates with a constant or time-dependent rotational speed of Ω around its symmetry axis (in the ϕ-direction). The inner sphere wall is kept at a constant high temperature, T_s, that is more than ambient temperature, $(T_s > T_\infty)$, whereas the bounded boundary of water is assumed adiabatic. As shown in Fig. 1, the immersion angle (θ_i) is defined as a symmetrical angle relative to the vertical axis of symmetry and is the angular distance from this axis to the intersection point of the sphere and interface. Furthermore, r indicates the radial component of the spherical coordinate measuring from the sphere's surface. Tables 1 and 2 list the physical parameters and thermophysical properties values, respectively. According to Table 1, the values of contact angle (θ_c) in all simulation cases are less than 90 degrees, revealing that the sphere's surface is hydrophilic.

Governing equations

The numerical simulation of the present study is performed using the Volume of Fluid (VOF) method [39]. The surface tension effect is incorporated in the VOF method. In this method, two or more phases do not interpenetrate. Also, the volume fraction of each additional phase must be considered in the computation. The governing equations used in this investigation are summarized in Table 3. Interface tracking between the phases can be done by solving a transport equation (Eq. (1)), where the source term (S_{a_q}) in this equation is zero. Furthermore, in each control volume, the sum of the volume fractions of all phases should be equal to 1. The value of a_q in each cell must range between 0 and 1. The value of $a_q = 1$ indicates a cell that is filled with fluid, $0 < a_q < 1$ indicates a cell that is partially filled

Table 3: Summary of the governing equations [43].

Equation	No.
Transport equation: $\frac{\partial a_q}{\partial t} + U\nabla a_q = \frac{S_{a_q}}{\rho_q}$	(1)
Mixture physical properties (density): $\rho = \sum_{q=1}^{n} a_q \rho_q$	(2)
Continuity equation: $\nabla . U = 0$	(3)
Momentum equation: $\frac{\partial(\rho U)}{\partial t} + \nabla.(\rho UU) = -\nabla p + \rho g + \mu\nabla^2 U + F_s$	(4)
Energy equation: $\frac{\partial(\rho E)}{\partial t} + \nabla.[U(\rho E + p)] = \nabla.(k_{eff}\nabla T) + S_e$	(5)
$E = \frac{\sum_{q=1}^{n} a_q \rho_q E_q}{\sum_{q=1}^{n} a_q \rho_q}$	(6)
Surface tension: $p_1 - p_2 = \sigma(\frac{1}{R_1} + \frac{1}{R_2})$	(7)
Wall adhesion: $\hat{n} = \hat{n}_w \cos\theta_c + \hat{t}_w \sin\theta_c$	(8)

with qth fluid, and $a_q = 0$ indicates a cell that is empty. The physical properties used in the transport equation (Eq. (1)), such as density is specified by Eq. (2) in each cell. In this study, the fluids are considered to be Newtonian, incompressible, immiscible, and quiescent. Moreover, the effect of temperature changes on thermophysical properties is negligible. The Reynolds number in this work is less than 8.2×10^6, which indicates that the flow is laminar [40, 41]. The continuity and momentum equations are presented in Eqs. (3) and (4), respectively. In Eq. (4), U is the velocity vector of the mixture, t the time, P the pressure, F_s the volumetric force at the interface resulting from surface tension, and μ, ρ are the dynamic viscosity and density, respectively. Furthermore, the energy equation is written as Eq. (5), where k_{eff} , S_e are the effective thermal conductivity and the source term, respectively. The problem geometry has a symmetry in the ϕ-direction, and therefore is considered axisymmetric. So, in the mentioned equations, derivatives in the ϕ -direction are removed $(\frac{\partial}{\partial\phi} = 0)$. For surface tension and wall adhesion simulation, the Continuum Surface Force (CSF) and wall adhesion models of *Brackbill et al*. [42] are used (Eq. (7) and (8)). The surface tension is formulated by the pressure drop across the surface, $p_1 - p_2$, which depends on the surface curvature as specified by two radii in orthogonal directions, R_1 and R_2, and the surface tension coefficient, σ (Eq. (7)). Also, i n Eq. (8), $\hat{n}_w$, $\hat{t}_w$, and θ_c are the normal, tangent unit vectors to the wall, and the contact angle at the wall, respectively.

Boundary conditions

According to Fig. 1, the geometry of the present problem is axisymmetric. Hence, numerical simulation is only performed for the right region of the domain. Three different function types are used for the rotational speed of the sphere. The first type is a uniform rotational speed as below:

$$\Omega = 2500 \quad (9)$$

The second type is resulted by adding a uniform rotational speed to a sinusoidal time-dependent pulsation as follows:

$$\Omega = 2500 + 500\sin(100\pi t) \quad (10)$$

The third type of time-dependent rotational speed is an exponential function as below:

$$\Omega = 2500\exp(-t) \quad (11)$$

The boundary conditions are: no-slip, no penetration, and isothermal conditions for the sphere's surface, no-slip, no penetration, and adiabatic conditions for the bounded boundary of liquid, and pressure-outlet condition at the upper boundary of the problem domain (in contact with gas).

NUMERICAL PROCEDURE

The governing equations along with the boundary condition are solved numerically with the finite volume solution method using the ANSYS Fluent (version 19.2). The upwind scheme with second-order accuracy is used for momentum and energy equations discretization. The pressure-velocity coupling is handled by the PISO (pressure implicit splitting of operators) algorithm. Moreover, the solver implements the VOF two-phase algorithm coupled with the level set method for the computations, which enables the capturing of liquid surface deformations. The pressure correction equation and the volume fraction discretization are treated by the pressure staggering option (PRESTO!) and the Compressive schemes, respectively. The body force formulation is performed by the implicit scheme. In each time step, the time-dependent parameter values are calculated from their values at previous time steps. By repeating this procedure and placing these values in discretized equations until the convergence criterion, the corrected values are derived at this time step. This solution process is repeated for the next time step. In addition, the CPU time for 128000 iterations is about 20 hours and the convergence criterion applied in all computations is 10^{-6}. Also, the residual error curves are indicated in Fig. 2.

Grid independency

Based on Table 1, the selected case to perform the mesh independence study is case 1 with a uniform rotational speed of Ω = 2500 $[rpm]$ (Eq. (9)). The mesh

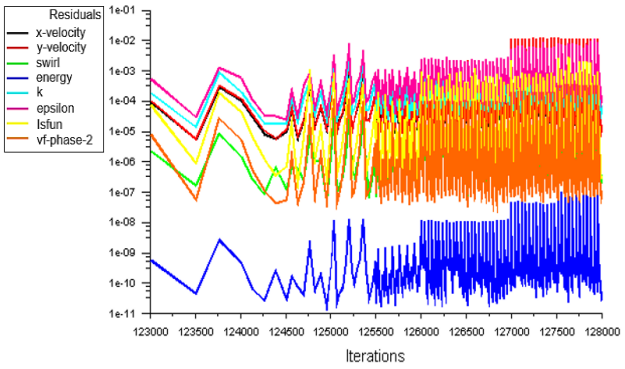

Fig. 2: Residual error curves.

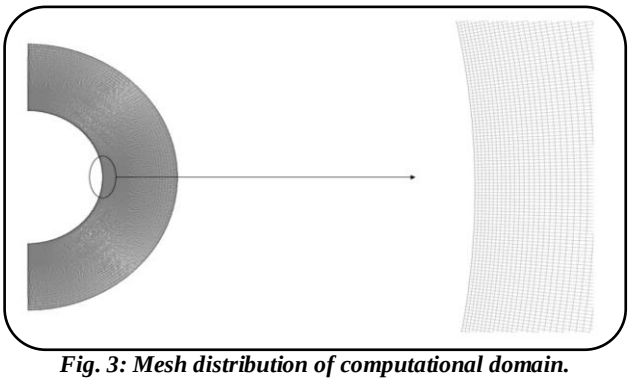

Fig. 3: Mesh distribution of computational domain.

distribution of the computational domain is depicted in Fig. 3. In this investigation, a non-uniform structural quad mesh is generated. Four different meshes namely, 4641, 18081, 44931, and 67264 are employed to conduct the independence test. The corresponding values of $< Nu_{Avg} >$ are shown in Table 4. A grid of 44931 is sufficiently fine to ensure the mesh independent solution so that the deviation of the $< Nu_{Avg} >$ between mesh numbers 3 and 4 is about 0.2%. Hence, this grid is selected to conduct all numerical calculations.

Time-step independency

In order to perform the time-step independence study, the time history of $< Nu_{Avg} >$ for case 1 with a uniform rotational speed of Ω = 2500 $[rpm]$ (Eq. (9)) under different time steps is presented in Table 5. As can be seen from Table 5, the variation of $< Nu_{Avg} >$ between time-step numbers 3 and 4 is about 0.3%. Hence, time-step 3 is selected to perform all calculations.

Furthermore, three mentioned independence tests were conducted for other rotational speeds with sine and exponential functions (Eqs. (10) and (11)), which yielded similar results to the uniform rotational speed (Eq. (9)).

Table 4. Mesh independence study.

Mesh No.	Total. No. of cells	$< \mathrm{Nu_{Avg}} >$	Deviation (%)
1	4641	1521.9843	–
2	18081	1901.8716	24.96
3	44931	2030.4381	6.76
4	67264	2034.9051	0.22

Table 5: Time-step independence study.

Time-step No.	Δt (s)	$< \mathrm{Nu_{Avg}} >$	Deviation (%)
1	7.2×10^{-4}	1473.8722	–
2	3.6×10^{-4}	1876.3867	27.31
3	1.8×10^{-4}	2030.4381	8.21
4	0.9×10^{-4}	2036.9355	0.32

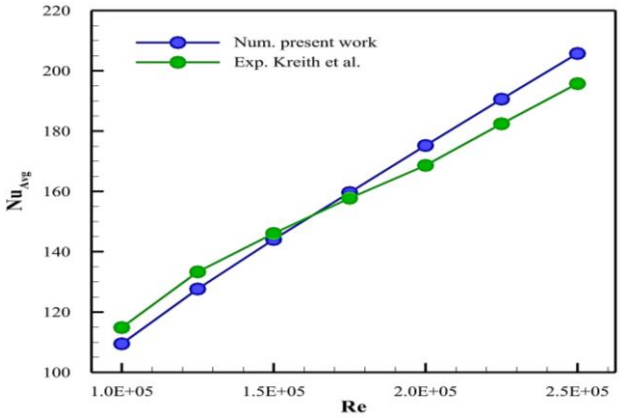

Fig. 4. Comparison of the surface-averaged Nusselt numbers from present investigation with those of previous experimental work [34] for various Reynolds numbers.

Validation study

In order to validate the numerical model, we conducted a literature survey to find similar results with the present investigation. Unfortunately, no work exactly describing the current problem is available for this configuration. Thus, the problem of a fully immersed rotating sphere with constant rotational speed is chosen to validate the numerical model. The surrounding fluid is air and the temperature of air and sphere's surface are 3000 [K] and 570 [K], respectively. Moreover, the range of Reynolds number is between 100000 and 250000. As can be seen from Fig. 4, the variations of surface-averaged Nusselt number (Nu_{Avg}) with Reynolds number (Re) are in good agreement with the experimental results of *Kreith et al.* [34]. The maximum difference in the results is less than 5%. So, this validation makes a good confidence in the current solution method and the robustness of our numerical model.

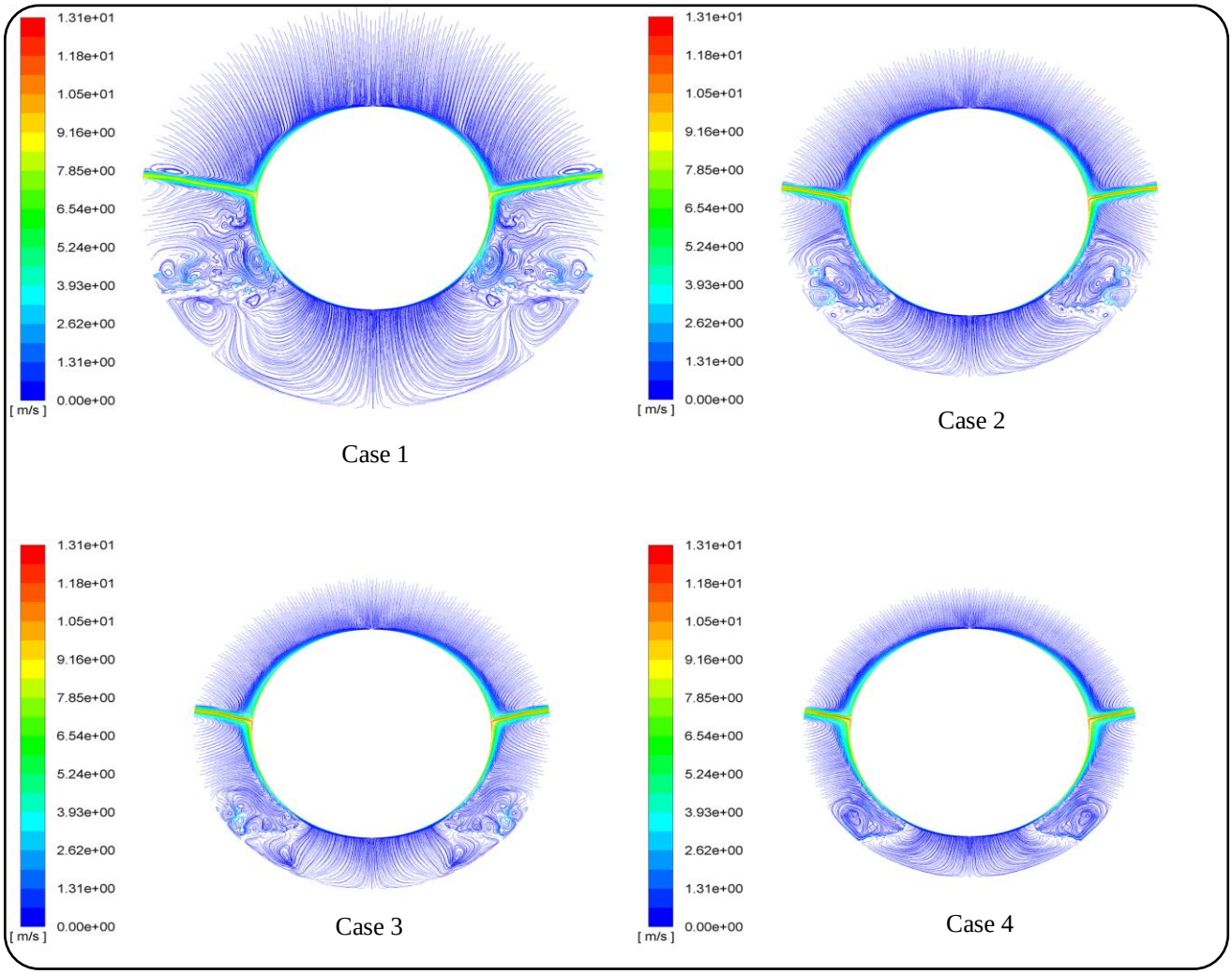

Fig. 5: Streamline patterns around sphere for different boundary radiuses Case 1) $R_\infty = 10$ [cm], Case 2) $R_\infty = 8$ [cm], Case 3) $R_\infty = 7.5$ [cm], and Case 4) $R_\infty = 7$ [cm].

ESULTS AND DISCUSSION

In this section, numerical investigations are carried out and discussed for various parameters. The results are presented in terms of streamlines, isotherms, volume fraction contours along with the film thickness, local and average Nusselt numbers. Moreover, the results are compared in a fixed time for all cases.

Streamline patterns and velocity vectors

The streamlines, velocity vectors, isotherms, and volume fraction contours for different cases with a uniform rotational speed of Ω = 2500 [rpm] (Eq. (9)) are shown in Figs. 5-8, respectively. The streamlines pattern and velocity vectors for various boundary radiuses are depicted in Fig. 5 and Fig. 6, respectively. The physical details of various cases are summarized in Table 1. In this investigation, a primary meniscus of the water film is formed on the sphere's surface because this surface is hydrophilic ($\theta_c = 40° < 90°$). Hence, as shown in Fig. 5 and Fig. 6, the water is drawn up the sphere' lower pole due to the centrifugal force generated by the rotation and its motion continues because of the water film formation. As the increase in the sphere radius stops, the water film motion ceases. Next, the water film is radially thrown out because of the inertial forces' dominance so that this ejection is shaped by capillary forces. As shown in Fig. 5 and Fig. 6, the ejection of water film from the sphere's equator in cases 2-4 is faster than case 1. This is due to lower interactions between water and air in the cases with smaller boundary radius. Also, the interactions between water and air phases produce vortices at the interface. However, most vortices are generated within the air phase that are unrelated to the water film motion.

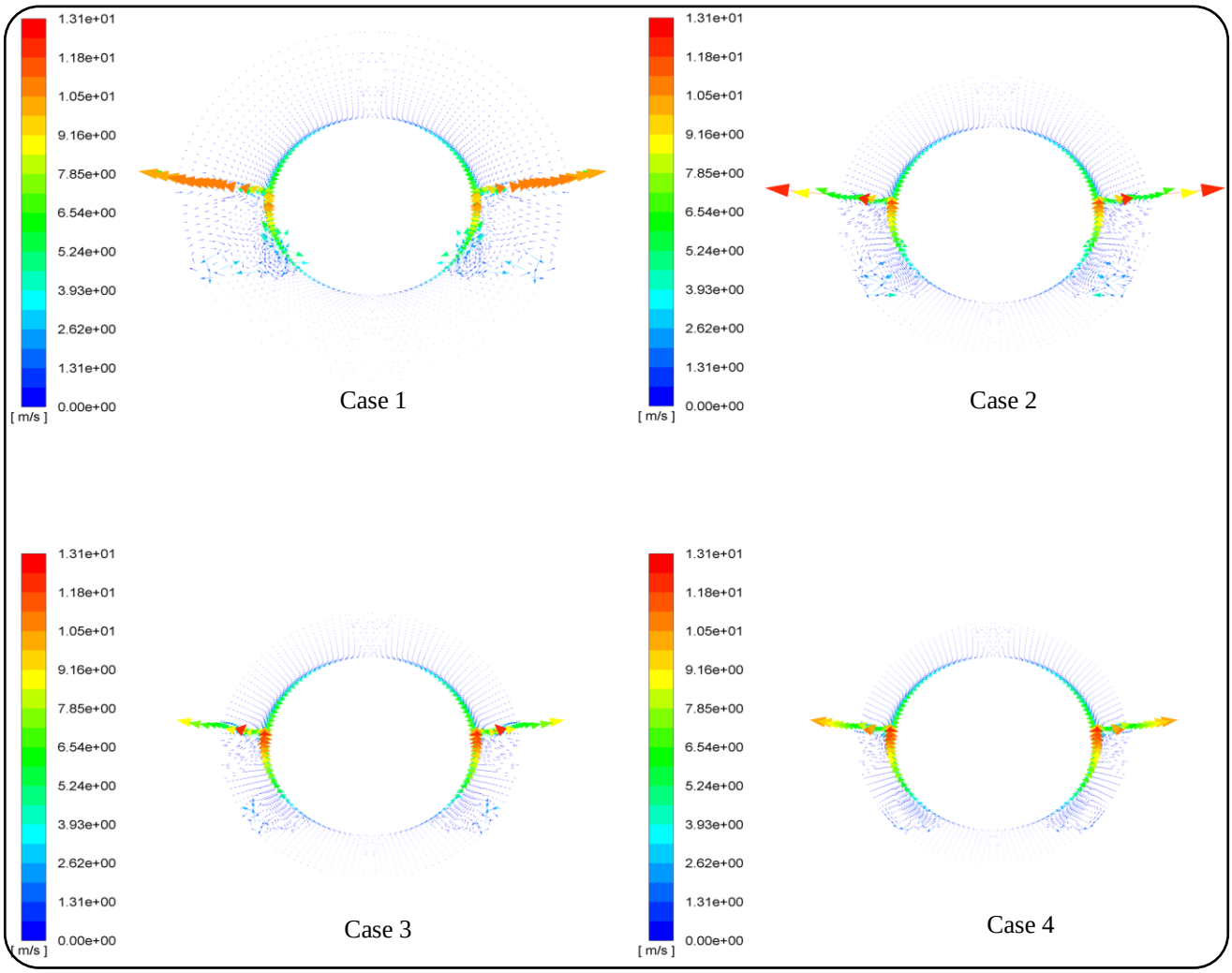

Fig. 6: Velocity vectors around sphere for different boundary radiuses Case 1) $R_\infty = 10$ [cm], Case 2) $R_\infty = 8$ [cm], Case 3) $R_\infty = 7.5$ [cm], and Case 4) $R_\infty = 7$ [cm].

Isotherm contours

The isotherm contours for various boundary radiuses are depicted in Fig. 7. The initial temperature of the mixture is 298.15 [K], which is lower than the sphere's surface temperature (333.15 [K]). Thus, as shown in Fig. 7, there are maximum gradients of temperature close to the surface. Furthermore, the isothermal layers in the air phase are thicker than the water phase because the specific heat capacity of air is lower than water. The motion of the water film close to the surface leads to an increase in its temperature. The heat transfer dominant mechanism in the equator is forced convection. However, the diffusion mechanism is stronger than convection outside this area.

Volume fraction contours

For the purpose of better observation of the water film motion on the surface, the volume fraction contours for various boundary radiuses are shown in Fig. 8. As can be seen, the water film becomes thicker by increase in boundary radius so that case 1 has the highest film thickness among various cases. This is because of stronger intermolecular adhesion forces in large boundary radiuses resulting from the higher volume of water in these cases. Moreover, the interface between air and water becomes more flatter by increase in boundary radius due to high water volume in large boundary radiuses.

Average and local Nusselt number

In this part, the effects of various boundary radiuses and different function types of rotational speed of the sphere on the Nusselt number are studied. The temporal variations of the surface-averaged Nusselt number (Nu_{Avg})

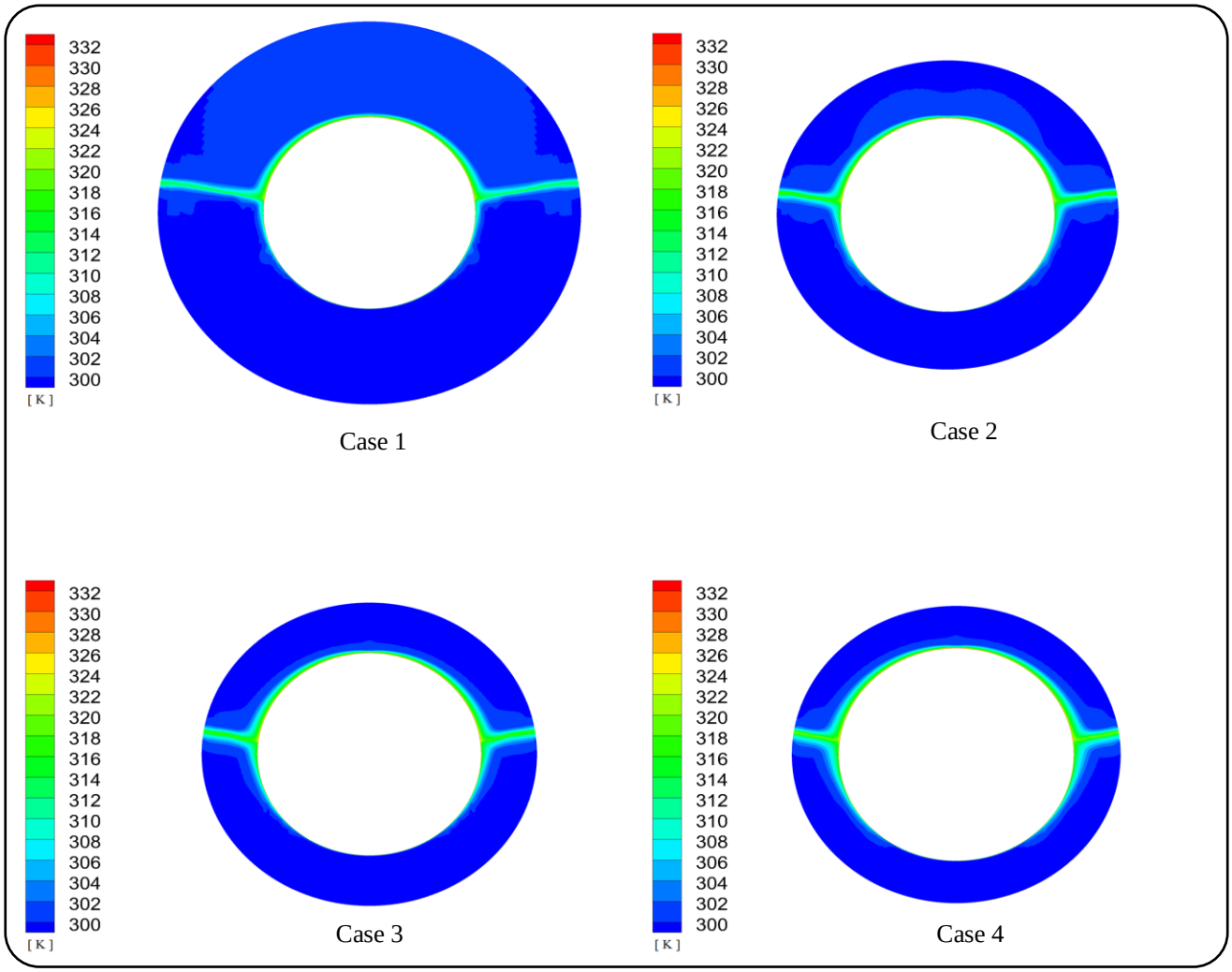

Fig. 7: Isotherm contours around sphere for different boundary radiuses Case 1) $R_\infty = 10$ [cm], Case 2) $R_\infty = 8$ [cm], Case 3) $R_\infty = 7.5$ [cm], and Case 4) $R_\infty = 7$ [cm].

with the boundary radius under various types of rotational speed are depicted in Fig. 9. Different cases under uniform (Eq. (9)), sinusoidal time-dependent pulsation (Eq. (10)), and exponential (Eq. (11)) functions for the rotational speed are compared in Fig. 9(a), (b), and (c), respectively. As can be seen from these figures, by increasing in time the values of Nu_{Avg} decrease for all types of rotational speed. This is because of ejecting water flow from the sphere's equator and the temperature rising of water film close to the surface over time. By ejecting the water film, air replaces it, which reduces the heat transfer rate due to lower heat capacity than water. Furthermore, according to Fig. 9, the values of Nu_{Avg} become larger by increase in boundary radius so that case 1 has the highest values of Nu_{Avg} among various cases. This is because of high water volume in large boundary radiuses, which increases the heat transfer rate.

The variations of the local Nusselt number (Nu_θ) along the sphere's surface for different boundary radiuses under various types of rotational speed are shown in Fig. 10. Based on this figure, the values of Nu_θ for larger boundary radiuses are higher than smaller ones in all types of rotational speed. Moreover, by moving along the surface from $\theta = 0°$ to $\theta = 45°$ (between lower pole and immersion angle position of the sphere), the values of Nu_θ increase. This trend is because the heat transfer rate of water close to the surface is more than air in this angular distance. Next, the air phase is added to the mixture, which leads to a significant reduction in the values of Nu_θ. Finally, by ejecting water film from the sphere's equator,

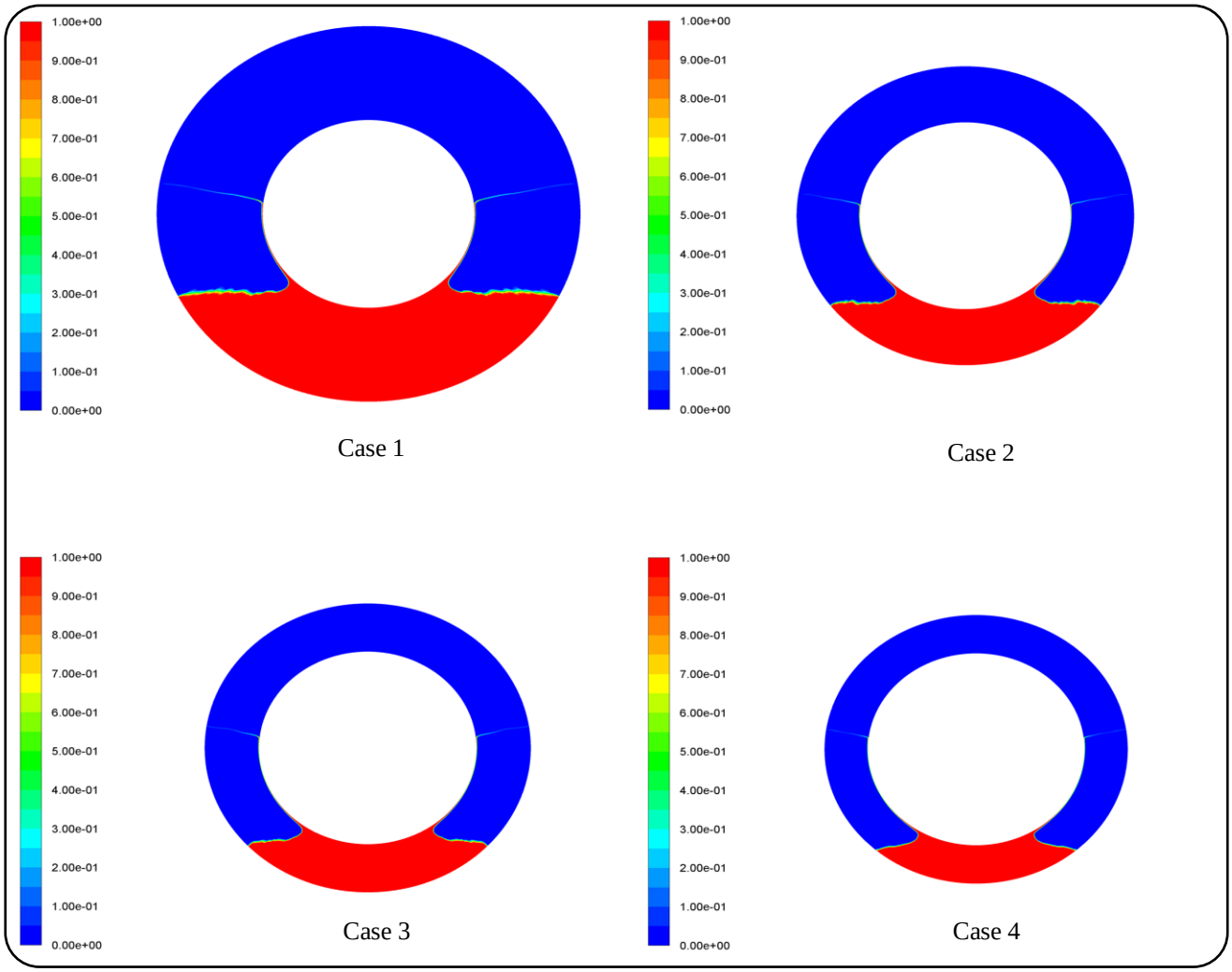

Fig. 8: Contours of water volume fraction around sphere for different boundary radiuses Case 1) $R_\infty = 10$ [cm], Case 2) $R_\infty = 8$ [cm], Case 3) $R_\infty = 7.5$ [cm], and Case 4) $R_\infty = 7$ [cm].

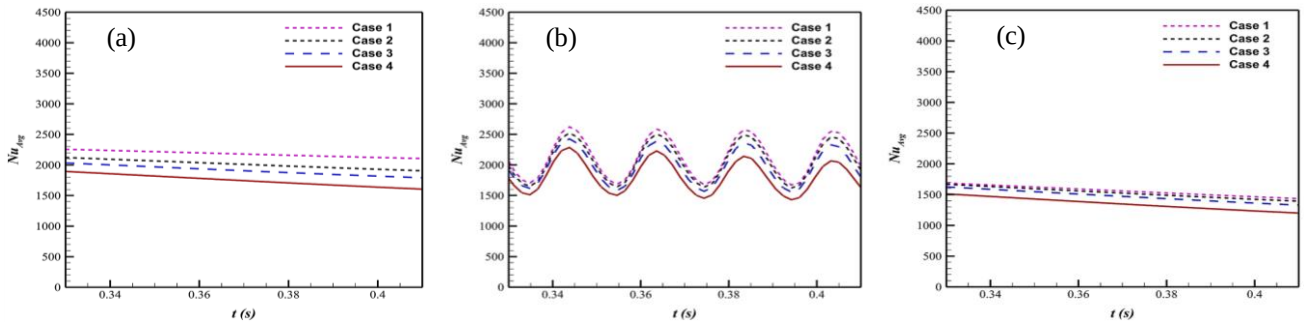

Fig. 9: Effects of the boundary radiuses and different function types of rotational speed on the temporal variations of the surface-averaged Nusselt number (Nu_{Avg}) (a) Eq. (9) (b) Eq. (10) (c) Eq. (11).

the Nu_θ values reach close to zero, which is due to the lower heat transfer rate of air than water.

The values of the time-surface-averaged Nusselt number ($< Nu_{Avg} >$) in various boundary radiuses and different types of rotational speed are presented in Table 6. According to this table, the values of $< Nu_{Avg} >$ increase

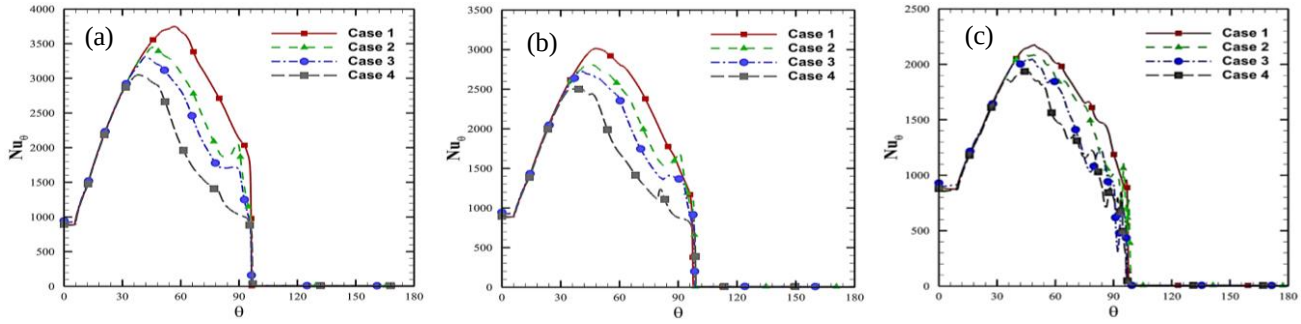

Fig. 10: Comparison of local Nusselt number (Nu_θ) distribution along the surface for various boundary radiuses under different types of rotational speed (a) Eq. (9) (b) Eq. (10) (c) Eq. (11).

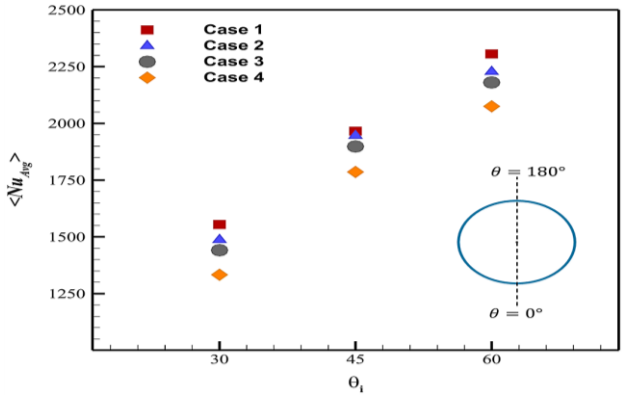

Fig. 11. Effects of the boundary radius and immersion angle (θ_i) on the time-surface-averaged Nusselt number ($< Nu_{Avg} >$) under uniform rotational speed of the sphere (Eq. (9)).

with increase in boundary radius so that case 1 has the highest values of $< Nu_{Avg} >$ among various cases for all types of rotational speed. As mentioned earlier, this is due to the higher volume of water in large boundary radiuses, which increases the heat transfer rate in these cases. Also, the effect of different types of rotational speed, including uniform (Eq. (9)), sinusoidal time-dependent pulsation (Eq. (10)), and exponential (Eq. (11)) functions on $< Nu_{Avg} >$ are compared in Table 6. The results indicate higher heat transfer performance of sinusoidal pulsation rotational speed (Eq. (10)) than other functions. Therefore, maximum variation in $< Nu_{Avg} >$ for Eq. (10) as a result of increasing the boundary radius from $R_\infty = 7$ [cm] (Case 4) to $R_\infty = 10\ [cm]$ (Case 1) is 10.3%. Furthermore, this increase is 35.5% for exponential function (Eq. (11)) compared to the sinusoidal pulsation rotational speed (Eq. (10)), which is due to higher rotational speeds of sinusoidal pulsation than the exponential function.

The effect of immersion angle (θ_i) on $< Nu_{Avg} >$ for different boundary radiuses under uniform rotational speed of the sphere (Eq. (9)) is shown in Fig. 11. According to the figure, as the immersion angle increases from $\theta_i = 30°$ to $\theta_i = 60°$, the values of $< Nu_{Avg} >$ increase about 51% on average. This is due to more contact between the water and surface at higher immersion angles.

Table 6: Effects of the boundary radius and different types of rotational speed on the time-surface-averaged Nusselt number ($< Nu_{Avg} >$).

	Eq. (9)	Eq. (10)	Eq. (11)
Case 1	1965.438	2006.225	1583.537
Case 2	1945.898	1995.966	1574.343
Case 3	1898.557	1936.931	1541.319
Case 4	1785.558	1819.379	1480.517

Film thickness

The changes in the thickness of the water film (δ) on the surface for various boundary radiuses and different types of rotational speed are shown in Fig. 12. According to this figure, the values of δ increase with increase in boundary radius so that case 1 has the highest thickness among various cases for all types of rotational speed. This is because of stronger intermolecular adhesion forces in large boundary radiuses resulting from the higher volume of water in these cases. Also, by moving along the surface, the values of δ decrease in all types of rotational speed due to a reduction in the intermolecular adhesion forces. Near the sphere's equator ($\theta = 90°$), this trend ceases and water film thickness increases because of the film movement stopping and accumulation of water in this region.

CONCLUSIONS

In this work, a numerical model is used to investigate the flow and heat transfer from a partially immersed rotating sphere in a bounded boundary of water with variable radius.

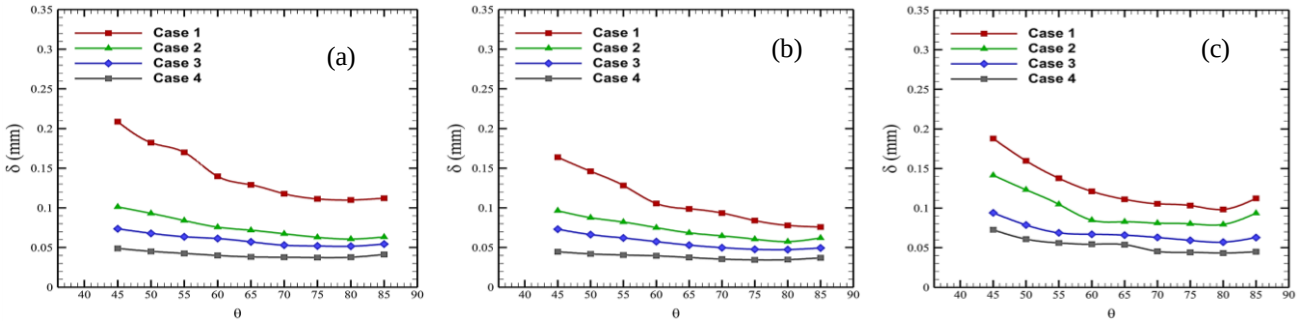

Fig. 12. The water film thickness (δ) distribution along the surface for various boundary radiuses under different types of rotational speed (a) Eq. (9) (b) Eq. (10) (c) Eq. (11).

The two-phase VOF model is applied to solve the governing equations. The analysis is carried for different boundary radiuses under various types of rotational speed of the sphere. The main results can be summarized as:

- The water is drawn up the sphere lower pole because of the centrifugal force generated by the rotation, and its motion continues due to the water film formation. Then, the water film is radially thrown out because of the inertial forces dominance.
- There is a little interaction between air and water in small boundary radiuses.
- There are maximum gradients of temperature near the surface of the sphere.
- The heat transfer dominant mechanism in the equator is forced convection. However, the diffusion mechanism is stronger than convection outside this area.
- By increasing in time, the values of surface-averaged Nusselt number decrease for all types of rotational speed. Moreover, these values become larger by increase in boundary radius.
- The values of local Nusselt number along the sphere's surface for larger boundary radiuses are higher than smaller ones in all types of rotational speed.
- The values of time-surface-averaged Nusselt number increase with increase in boundary radius and the sinusoidal pulsation rotational speed (Eq. (10)) indicates higher heat transfer performance among various rotational speed functions.
- Maximum change in time-surface-averaged Nusselt number for Eq. (10) due to increasing the boundary radius from $R_\infty = 7\ [cm]$ (Case 4) to $R_\infty = 10\ [cm]$ (Case 1) is 10.3%. Moreover, this increase is 35.5% for exponential function (Eq. (11)) compared to the sinusoidal pulsation rotational speed (Eq. (10)).
- In the case of a uniform rotational speed of the sphere (Eq. (9)), as the immersion angle increases from $\theta_i = 30°$ to $\theta_i = 60°$, the values of time-surface-averaged Nusselt number increase about 51% on average due to more contact between the water and surface at higher immersion angles.
- By increasing in boundary radius, the thickness of the water film increases for all types of rotational speed. Furthermore, these values become smaller by moving along the surface in all types of rotational speed due to a reduction in the intermolecular adhesion forces.

Nomenclature

Volume fraction of each phase $(-)$	a_q
Specific heat capacity $(J/kg.K)$	C_p
Energy (J)	E
Volumetric forces resulting from surface tension (N)	F_s
Gravitational constant (m/s^2)	g
Average convection heat transfer coefficient $(W/m^2.K)$	h_{Avg}
Time-averaged convection heat transfer coefficient $(W/m^2.K)$	$< h_{Avg} >$
Local convection heat transfer coefficient $(W/m^2.K)$	h_θ
Thermal conductivity $(W/m.K)$	k
Surface normal gradient of a $(-)$	n
The unit vectors normal to the wall $(-)$	n_w
Surface-averaged Nusselt number $(-) = h_{Avg}D/k = \frac{1}{s}\int_s Nu_\theta ds$	Nu_{Avg}
Time-surface-averaged Nusselt number $(-) = < h_{Avg} > D/k = \frac{1}{t}\int_0^t Nu_{Avg} dt$	$< Nu_{Avg} >$
Local Nusselt number $(-) = h_\theta D/k$	Nu_θ
Pressure (N/m^2)	p

Prandtl number $(-) = C_p\mu/k$	Pr
Solid sphere radius (cm), Radii in orthogonal direction (m)	R
Boundary radius (cm)	R_∞
Radial coordinate (cm)	r
Reynolds number $(-) = \Omega r^2/\nu$	Re
Source term $(-)$	S
Temperature (K)	T
Time (s)	t
The unit vectors tangential to the wall $(-)$	t_w
Velocity (m/s)	U
Subscripts	
Phase 1	1
Phase 2	2
Ambient	∞
Average	Avg
Contact	c
effective	eff
Immersion	i
Phase	q
Surface of the sphere, Surface tension	s
wall	w
Greek symbols	
Water film thickness (mm)	δ
Acute angle subtended at the center of the sphere by any point and the nearest polar latitude coordinate (°)	θ
Contact angle (°)	θ_c
Immersion angle (°)	θ_i
Dynamic viscosity $(kg/m.s)$	μ
Kinematic viscosity (m^2/s)	ν
Density (kg/m^3)	ρ
Surface tension (N/m)	σ
Median angle coordinate (°)	ϕ
Rotational speed (rpm)	Ω

Received: May. 08, 2022 ; Accepted: Jul. 04, 2022

References

[1] Langley K.R., Maynes D., Truscott T.T., Eggs and Milk: Spinning Spheres Partially Immersed in a Liquid Bath, *Physics of Fluids*, **27(3):** 032102 (2015).

[2] von Karman T., Uber Laminare Und Turbulente Reibung, *Z. Angew. Math. Mech.*, **1:** 233-252 (1921).

[3] Nematollahzadeh A., Jangara H., Exact Analytical and Numerical Solutions for Convective Heat Transfer in a Semi-Spherical Extended Surface with Regular Singular Points, *Iranian Journal of Chemistry and Chemical Engineering (IJCCE)*, **40(3):** 980-989 (2021).

[4] Habibi M.R., Amini M., Arefmanesh A., Ghasemikafrudi E., Effects of Viscosity Variations on Buoyancy-Driven Flow from a Horizontal Circular Cylinder Immersed in Al_2O_3-Water Nanofluid, *Iranian Journal of Chemistry and Chemical Engineering (IJCCE)*, **38(1):** 213-232 (2019).

[5] Naseri Nia S., Rabiei F., Rashidi M.M., Kwang T.M., Lattice Boltzmann Simulation of Natural Convection Heat Transfer of a Nanofluid in a L-Shape Enclosure with a Baffle, *Results in Physics*, **19:** 103413 (2020).

[6] Rashidi M.M., Sadri M., Sheremet M.A., Numerical Simulation of Hybrid Nanofluid Mixed Convection in a Lid-Driven Square Cavity with Magnetic Field Using High-Order Compact Scheme, *Nanomaterials*, **11(9):** 2250 (2021).

[7] Zahmatkesh R., Mohammadiun H., Mohammadiun M., Dibaei Bonab M.H., Sadi M., Theoretical Investigation of Entropy Generation in Axisymmetric Stagnation Point Flow of Nanofluid Impinging on the Cylinder Axes with Constant Wall Heat Flux and Uniform Transpiration, *Iranian Journal of Chemistry and Chemical Engineering (IJCCE)*, **40(6):** 1893-1908 (2021).

[8] Mohammadiun H., Montazeri M., Mohammadiun M., dibaee bonab M.h., Vahedi M., Inverse Estimation of Time-Dependent Heat Flux in Stagnation Region of Annular Jet on a Cylinder Using Levenberg–Marquardt Method, *Iranian Journal of Chemistry and Chemical Engineering (IJCCE)*, **41(3):** 971-988 (2021).

[9] Majeed A., Amin N., Zeeshan A., Ellahi R., Sait S.M., Vafai K., Numerical Investigation on Activation Energy of Chemically Reactive Heat Transfer Unsteady Flow with Multiple Slips, *International Journal of Numerical Methods for Heat & Fluid Flow*, **30(11):** 4955-4977 (2020).

[10] Ellahi R., Alamri S.Z., Basit A., Majeed A., Effects of Mhd and Slip on Heat Transfer Boundary Layer Flow over a Moving Plate Based on Specific Entropy Generation, *Journal of Taibah University for Science*, **12(4):** 476-482 (2018).

[11] Goodarzi M., Tlili I., Moria H., Abdullah Alkanhal T., Ellahi R., Anqi A.E., Reza Safaei M., Boiling Heat Transfer Characteristics of Graphene Oxide Nanoplatelets Nano-Suspensions of Water-Perfluorohexane (C6F14) and Water-N-Pentane, *Alexandria Engineering Journal*, **59(6):** 4511-4521 (2020).

[12] Bhatti M.M., Ellahi R., Zeeshan A., Marin M., Ijaz N., Numerical Study of Heat Transfer and Hall Current Impact on Peristaltic Propulsion of Particle-Fluid Suspension with Compliant Wall Properties, *Modern Physics Letters B*, **33(35):** 1950439 (2019).

[13] Montazeri M., Mohammadiun H., Mohammadiun M., Dibaee Bonab M.H., Vahedi M., Inverse Analysis of the Time-Dependent Heat Flux in Stagnation Point Flow of Incompressible Fluid Impinging on a Cylinder with Uniform Surface Suction-Blowing Using Levenberg–Marquardt Method, *Inverse Problems in Science and Engineering*, **29(9):** 1219-1259 (2021).

[14] Bilal Ashraf M., Chemically Radiative Flow of Viscoelastic Fluid over Stretching Cylinder with Convective Condition, *Iranian Journal of Chemistry and Chemical Engineering (IJCCE)*, **40(5):** 1683-1692 (2021).

[15] Alsabery A.I., Selimefendigil F., Hashim I., Chamkha A.J., Ghalambaz M., Fluid-Structure Interaction Analysis of Entropy Generation and Mixed Convection inside a Cavity with Flexible Right Wall and Heated Rotating Cylinder, *International Journal of Heat and Mass Transfer*, **140:** 331-345 (2019).

[16] Wang T., Wang Z., Xi G., Huang Z., Periodic Unsteady Mixed Convection in Square Enclosure Induced by Inner Rotating Circular Cylinder with Time-Periodic Pulsating Temperature, *International Journal of Heat and Mass Transfer*, **111:** 1250-1259 (2017).

[17] Liao C.-C., Lin C.-A., Mixed Convection of a Heated Rotating Cylinder in a Square Enclosure, *International Journal of Heat and Mass Transfer*, **72:** 9-22 (2014).

[18] Sasmal C., Gupta A.K., Chhabra R.P., Natural Convection Heat Transfer in a Power-Law Fluid from a Heated Rotating Cylinder in a Square Duct, *International Journal of Heat and Mass Transfer*, **129:** 975-996 (2019).

[19] Kareem A.K., Gao S., Mixed Convection Heat Transfer of Turbulent Flow in a Three-Dimensional Lid-Driven Cavity with a Rotating Cylinder, *International Journal of Heat and Mass Transfer*, **112:** 185-200 (2017).

[20] Selimefendigil F., Öztop H.F., Mixed Convection of Nanofluids in a Three Dimensional Cavity with Two Adiabatic Inner Rotating Cylinders, *International Journal of Heat and Mass Transfer*, **117:** 331-343 (2018).

[21] Shirazi M., Shateri A., Bayareh M., Numerical Investigation of Mixed Convection Heat Transfer of a Nanofluid in a Circular Enclosure with a Rotating Inner Cylinder, *Journal of Thermal Analysis and Calorimetry*, **133(2):** 1061-1073 (2018).

[22] Souayeh B., Hdhiri N., Alam M.W., Hammami F., Alfannakh H., Convective Heat Transfer and Entropy Generation around a Sphere within Cuboidal Enclosure, *Journal of Thermophysics and Heat Transfer*, **34(3):** 605-625 (2020).

[23] Lee D., Jang H., Lee B.J., Choi W., Byon C., Internal Natural Convection around a Sphere in a Rectangular Chamber, *International Journal of Heat and Mass Transfer*, **136:** 501-509 (2019).

[24] Gallegos A.D., Málaga C., Natural Convection in Eccentric Spherical Annuli, *European Journal of Mechanics - B/Fluids*, **65:** 464-471 (2017).

[25] Chen Z., Yang L.M., Shu C., Zhao X., Liu N.Y., Liu Y.Y., Mixed Convection between Rotating Sphere and Concentric Cubical Enclosure, *Physics of Fluids*, **33(1):** 013605 (2021).

[26] D'Alessio S., An Analytical Study of the Early Stages of Unsteady Free Convective Flow from a Differentially Heated Rotating Sphere at Large Grashof Numbers, *International Journal of Computational Methods and Experimental Measurements*, **7(1):** 57-67 (2018).

[27] Jabari Moghadam A., Baradaran Rahimi A., A Numerical Study of Flow and Heat Transfer between Two Concentric Rotating Spheres with Time-Depenent Angular Velocities, *Scientia Iranica (Transaction B: Mechanical Engineering)*, **16(3):** 197-211 (2009).

[28] Jabari Moghadam A., Baradaran Rahimi A., Similarity Solution in the Study of Flow and Heat Transfer between Two Rotating Spheres with Constant Angular Velocities, *Scientia Iranica (Transaction B: Mechanical Engineering)*, **16(4):** 354-362 (2009).

[29] Hao X., Yang X., Peng C., Yao Z., Heat Transfer between Rotating Sphere and Spherical-Surface Heat Sink, *Journal of Thermal Analysis and Calorimetry*, **141(1):** 413-420 (2020).

[30] Zhang J., Zhen Q., Liu J., Lu W.-Q., Effect of Spacing on Laminar Natural Convection Flow and Heat Transfer from Two Spheres in Vertical Arrangement, *International Journal of Heat and Mass Transfer*, **134:** 852-865 (2019).

[31] Nigam S.D., Note on the Boundary Layer on a Rotating Sphere, *Zeitschrift für angewandte Mathematik und Physik ZAMP*, **5(2):** 151-155 (1954).

[32] Singh S.N., Heat Transfer by Laminar Flow from a Rotating Sphere, *Applied Scientific Research*, **9(1):** 197 (1960).

[33] Samad A., Garrett S.J., On the Laminar Boundary-Layer Flow over Rotating Spheroids, *International Journal of Engineering Science*, **48(12):** 2015-2027 (2010).

[34] Kreith F., Roberts L.G., Sullivan J.A., Sinha S.N., Convection Heat Transfer and Flow Phenomena of Rotating Spheres, *International Journal of Heat and Mass Transfer*, **6(10):** 881-895 (1963).

[35] Feng Z.-G., Direct Numerical Simulation of Forced Convective Heat Transfer from a Heated Rotating Sphere in Laminar Flows, *Journal of Heat Transfer*, **136(4):** (2014).

[36] Gutiérrez G., Fehr C., Calzadilla A., Figueroa D., Fluid Flow up the Wall of a Spinning Egg, *American Journal of Physics*, **66(5):** 442-445 (1998).

[37] Martinez J., Polatdemir E., Bansal A., Yifeng W., Shengtao W., Fluid Flow up a Spinning Egg and the Coriolis Force, *European Journal of Physics*, **27(4):** 805 (2006).

[38] Safarzadeh S., Rahimi A.B., Numerical Investigation of Flow and Heat Transfer from a Rotating Sphere with Constant Angular Velocity around Vertical Axis Floating in Stationary Fluid, *Journal of Heat Transfer*, **144(2):** (2021).

[39] Hirt C.W., Nichols B.D., Volume of Fluid (VOF) Method for the Dynamics of Free Boundaries, *Journal of Computational Physics*, **39(1):** 201-225 (1981).

[40] Kohama Y., Kobayashi R., Boundary-Layer Transition and the Behaviour of Spiral Vortices on Rotating Spheres, *Journal of Fluid Mechanics*, **137:** 153-164 (1983).

[41] Garrett S.J., Peake N., The Stability and Transition of the Boundary Layer on a Rotating Sphere, *Journal of Fluid Mechanics*, **456:** 199-218 (2002).

[42] Brackbill J.U., Kothe D.B., Zemach C., A Continuum Method for Modeling Surface Tension, *Journal of Computational Physics*, **100(2):** 335-354 (1992).

[43] Du W., Feng D., Xu J., Wei W., Computational Fluid Dynamics Modeling of Gas-Liquid Two-Phase Flow around a Spherical Particle, *Chemical Engineering & Technology*, **36(5):** 840-850 (2013).